EXPERIENCES WITH TERRESTRIAL LASER SCANNER MODELLING AND ACCURACY ASSESSMENT

Derek D Lichti [a] and Maria Gabriele Licht [b]

[a] Department of Spatial Sciences, Curtin University of Technology, GPO Box U1987, Perth, WA 6845, Australia, d.lichti@curtin.edu.au
[b] Institut für Photogrammetrie und Fernerkundung, Universität Karlsruhe (TH), Kaiserstrasse 12, 76131 Karlsruhe, Germany, licht@gik.uni-karlsruhe.de

Commission V, WG 3

KEY WORDS: Accuracy, Calibration, Error, Laser Scanning, LIDAR, TLS.

ABSTRACT:

This paper presents advances in terrestrial laser scanner systematic error modelling and self-calibration. The error model consists of 19 additional parameters grouped into two categories: physical and empirical. The physical group comprises known error sources such as rangefinder offset, cyclic errors, collimation axis error, trunnion axis error, vertical circle index error and others. The empirical terms lack ready physical explanation but nonetheless model significant errors. Results from self-calibration and an accuracy assessment experiment respectively show that up to 80% and 36% improvement was achieved as a result of using the correction models. Four other experiments designed to examine the influence of manufacturer's correction parameters and centroid software as well as instrument biases are also described. The results from these tests reveal significant biases in some cases.

1. INTRODUCTION

Attention to the problem of terrestrial laser scanner (TLS) calibration has increased in the last couple years. Among the first were Gielsdorf et al. (2004), who propose error models and a calibration method using planar targets for the low-cost TLS they constructed. Their parameter set includes terms for trunnion axis error, vertical index error, horizontal collimation error, additive rangefinder constant and eccentricity.

Amiri Parian and Grün (2005) exploit some of the common properties shared by panoramic cameras and TLSs. They report the use of 2D image point observations derived from the scanner data in an extended panoramic camera model calibration of the Z+F Imager 5003. Their residual analyses and accuracy assessment demonstrate considerable improvement as a result of their modelling. However, they only model angular systematic errors and not rangefinder errors.

Lichti and Franke (2005) approach the problem by recognising similarities between theodolites and TLSs. They present a seven-term additional-parameter error model and 3D free-network, self-calibration procedure. Up to 73% improvement in the RMS of residuals as a result of the modelling is demonstrated for the iQsun 880 laser scanner.

Abmayr et al. (2005) also address calibration of the Z+F Imager 5003 with error models originating from theodolite modelling. They propose a simple, non-simultaneous calibration method for estimating trunnion axis error, collimation axis error and vertical circle index error.

This paper presents advancements since Lichti and Franke (2005) in the modelling of the Faro 880 (previously known as the iQsun 880) and accuracy assessment. After discussing some of the pertinent characteristics of this instrument, the observation modelling approach is described and additional parameters are discussed with examples. Though the focus of this paper is on the Faro instrument, the models and calibration method are formulated in a general manner to allow application to other scanners. Experimental details and results of a test conducted to examine the accuracy improvement gained by using the estimated additional parameters are then given. Results from other relevant performance tests of the scanning system (i.e. instrument, targets and software) are followed by concluding remarks

2. OBSERVATION MODELLING

2.1 The Faro 880

The Faro 880 terrestrial laser scanner offers a near spherical field of view made possible by a 320° vertical angle scanning range and a 180° horizontal field of view. The rangefinder operates on the phase difference method (Rüeger, 1990) with three modulating wavelengths. The shortest is nominally 1.2 m and the other two differ by factors of 8: nominally 9.6 m and 76.8 m. The scanner features two orthogonal inclinometers that correct the captured data for instrument tilt. The manufacturer specifies 0.01° (36″) for the inclinometer accuracy and 3 mm linearity error at 10 m with 84% target reflectivity for the rangefinder.

Targets used for scan registration include spheres and a proprietary planar template that can be printed and mounted on a flat surface. The planar target comprises a white circle on a grey background with a black cross at the centre to allow independent co-ordination by total station. The accompanying iQscene software facilitates data capture with user-selected angular resolution and features data editing, target measurement, registration and import/export capabilities.

2.2 Observation Equations

The spherical co-ordinate observations of object space point i in scanner space j are range, ρ_{ij}, horizontal direction, θ_{ij}, and elevation (vertical) angle, α_{ij}, which are parameterised in terms of Cartesian, scanner space co-ordinates (x_{ij}, y_{ij}, z_{ij}) as follows

$$\rho_{ij} = \sqrt{x_{ij}^2 + y_{ij}^2 + z_{ij}^2} + \Delta\rho \tag{1}$$

$$\theta_{ij} = \arctan\left(\frac{y_{ij}}{x_{ij}}\right) + \Delta\theta \tag{2}$$

$$\alpha_{ij} = \arctan\left(\frac{z_{ij}}{\sqrt{x_{ij}^2 + y_{ij}^2}}\right) + \Delta\alpha \tag{3}$$

The spherical co-ordinates must be derived from the Cartesian co-ordinates exported by iQscene such that their range conforms to that of data acquisition, i.e. ($0° \le \theta_{ij} \le 180°$) and ($-70° \le \alpha_{ij} \le 250°$). The scanner space and object space co-ordinates are related by the three-dimensional rigid body transformation

$$\begin{bmatrix} x_{ij} \\ y_{ij} \\ z_{ij} \end{bmatrix} = R_3(\kappa_j)R_2(\phi_j)R_1(\omega_j)\left\{\begin{bmatrix} X_i \\ Y_i \\ Z_i \end{bmatrix} - \begin{bmatrix} X_{s_j} \\ Y_{s_j} \\ Z_{s_j} \end{bmatrix}\right\} \tag{4}$$

where (X_s, Y_s, Z_s) are the object space co-ordinates of scanner position j; (ω, ϕ, κ) are the Cardan angles for the rotation from object space to scanner space j; (X, Y, Z) are the object space co-ordinates of object point i; and R_1, R_2, R_3 are the matrices for rotation about the X-, Y- and Z-axes, respectively. These observation equations are augmented with respective systematic error correction models, $\Delta\rho$, $\Delta\theta$ and $\Delta\alpha$, which constitute the interior orientation of the scanner and are assumed to be block invariant for self-calibration. Since the scanner's inclinometer data are used to remove the effects of instrument tilt, the following two parameter observations of the "levelling" angles can be introduced for self-calibration

$$\begin{aligned} \omega_j &= 0 \\ \phi_j &= 0 \end{aligned} \tag{5}$$

3. ADDITIONAL PARAMETERS

3.1 Systematic Error Modelling

The problem underlying TLS self-calibration is that of model identification. Some systematic error sources, such as those common to total stations, can be expected *a priori* and are referred to herein as the physical parameters. In contrast, the physical interpretation of others, the empirical parameters, is not necessarily apparent. These are inferred from systematic trends visible in the residuals of a highly-redundant and geometrically strong, minimally-constrained least-squares adjustment. The current additional parameter (AP) model consists of 19 coefficients: 8 for range, 7 for horizontal direction and 4 for elevation angle. Each term is listed in Tables 1 and 2 and is described below. All errors described herein have been observed in several calibration datasets captured over the course of 12 months. Generally speaking, the physical parameters are the most significant.

AP(s)	Explanation
a_0	Rangefinder additive constant
a_3 and a_4	Cyclic error with nominal period of 0.6 m
a_5 and a_6	Cyclic error with nominal period of 4.8 m
b_1	Collimation axis error
b_2	Trunnion axis error
b_3 and b_4	Non-orthogonality of the plane containing the horizontal angle encoder and vertical axis
b_5	Horizontal direction encoder scale error
c_0	The vertical circle index error
c_2	Vertical eccentricity error

Table 1. Physical APs.

AP(s)	Explanation
a_2	Sinusoidal error in range as a function of elevation angle
a_7 and a_8	Sinusoidal error in range as a function of horizontal direction
b_6 and b_7	First and second sinusoidal errors in horizontal direction as a function of elevation angle
c_3 and c_4	Sinusoidal error in elevation angle as a function of horizontal direction

Table 2. Empirical APs.

3.2 Physical Parameters

3.2.1 Range APs. The rangefinder additive correction is modelled as a constant and applies to the Faro instrument/planar-target combination. No scale term (a_1) is included in the model since its estimation requires inclusion of an independent scale definition in the self-calibration network.

There are two sets of cyclic error terms: the usual two (a_3, a_4) to model errors at the finest unit length (half the finest modulating wavelength) and two (a_5, a_6) for the errors at half the median wavelength. Un-modelled errors due to the former have a wavelength of 0.6 m and are pictured in the residual (v) plot of Figure 1. The median-wavelength (λ=4.8 m) cyclic error, was found to be of much smaller magnitude and does not exhibit high repeatability from one calibration dataset to the next. Thus these two terms are excluded from the model hereafter.

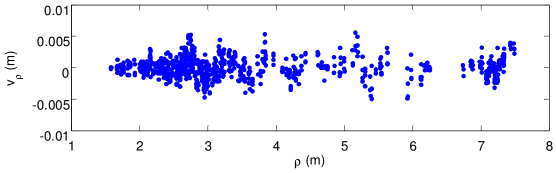

Figure 1. Fine wavelength cyclic error in range residuals.

Existence of cyclic errors having modulating wavelengths other than the shortest has been reported elsewhere, though. Covell and Rüeger (1982) report cyclic errors due to electrical cross-talk having period equal to the half of that of the coarse modulating wavelength for several EDM instruments in addition to those at the fine wavelength. For the system examined here there also exists the possibility of cyclic errors with nominal period of 38.4 m, but longer-range testing is required to examine this.

3.2.2 Horizontal Direction APs. Two of the largest angular errors sources are the collimation axis (b_1) and trunnion axis (b_2) errors, which respectively vary with the secant and the tangent of elevation angle. The non-orthogonality of the plane containing the horizontal angle encoder and the vertical axis is manifest as a sinusoidal error with period 180°. Lichti and Franke (2005) parameterise it in terms of its amplitude and phase. It has been recast here in terms of the two orthogonal (i.e. sine and cosine) coefficients: b_3 and b_4. The principal advantages of this new parameterisation are:

- Approximate parameter values are not required since the model is linear;
- Convergence of the self-calibration adjustment is more rapid than with the non-linear model; and
- From an algorithmic standpoint, individual coefficients are more easily eliminated if found to be statistically insignificant.

The b_5 term models a scale error in horizontal direction. A complete error model might also include two coefficients for horizontal circle eccentricity. These have been excluded simply because they were not found to be necessary for any of the four datasets reported on thus far, though significant vertical circle eccentricity has been found, as discussed below.

3.2.3 Elevation Angle APs. The first term is the vertical circle index error, c_0. The c_2 term models a sinusoidal error in elevation angle with a period of 360º, which suggests eccentricity error. It is pictured in the residual plot of Figure 2. Only one term (sine) is included in the model. The corresponding cosine term is nearly perfectly correlated (i.e. 0.98) to certain positional and rotational elements of the exterior orientation and, therefore, omitted from the AP model.

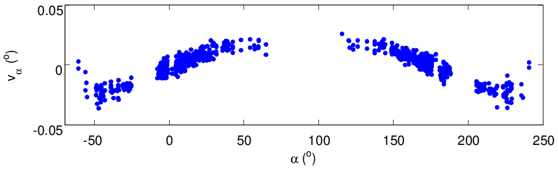

Figure 2. Vertical eccentricity error in elevation angle residuals.

3.3 Empirical Parameters

3.3.1 Range APs. The sinusoidal error in range (a_2) is hypothesised to be due to a vertical offset between the laser and trunnion axes (Lichti and Franke, 2005). Though simulation confirmed this as a plausible physical cause, it is still regarded an empirical parameter. The terms a_7 and a_8 model a sinusoidal error in range as a function of horizontal direction with period 90°. Its physical cause is not known but is more than likely linked to the horizontal scanning mechanism.

3.3.2 Horizontal Direction APs. The terms b_6 and b_7 model errors in horizontal direction as a function of elevation angle. Their respective periods are 120° and 90°.

3.3.3 Elevation Angle APs. The c_3 and c_4 terms model a sinusoidal error as a function of horizontal direction with period of 120º—the angular separation between instrument support holes in the tribrach—as pictured in Figure 3. One possible cause of this error is mechanical wobble of the instrument in its tribrach as it rotates about its vertical axis, as Kersten et al. (2005) found for a Mensi laser scanner. Our scanner has been consistently observed to go slightly off level (as indicated by the tribrach's bull's eye bubble) upon completion of the 180° horizontal scan, so this is indeed a plausible cause.

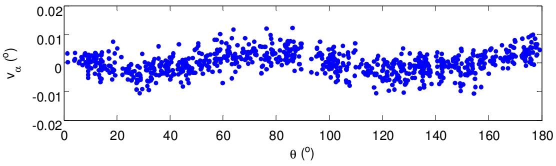

Figure 3. Periodic error in elevation angle residuals.

4. ACCURACY TESTING

4.1 Experiment Description

Similar to the experiment described by Lichti and Franke (2005), an eight-scan self-calibration network with 131 planar, A4-size Faro targets mounted on all 4 walls, the floor and the ceiling of a 12 m x 9 m x 3.3 m room was observed in December 2005. Four scans were captured at two nominal scanner locations separated by 6.7 m. The instrument was manually rotated on the tripod by 90° after each scan of the set of four was captured. As with all experiments described herein, the angular sampling interval was set to 0.044° (≈8 mm at 10 m range). The size of the room limited the maximum range to approximately 10 m.

Target centre measurement was performed using the "contrast centroiding" tool within iQscene. Spherical co-ordinate observations were derived from the Cartesian co-ordinates exported from iQscene. The ensuing free network, self-calibration adjustment (performed with software composed by the first author) had 2193 observations and 1738 degrees-of-freedom. Inclinometer observations were not used for this calibration. Variance component estimation was used to optimise the contribution of each of the three groups of observables. The respective RMS of residuals for the range, horizontal direction and elevation angle groups with and without self-calibration are given in Table 3. Clearly all variables were significantly improved due to the calibration, with the angles benefiting the most.

	Without Self-Calibration	With Self-Calibration	% Improvement
RMS ρ (m)	±0.0023	±0.0012	48
RMS θ (°)	±0.0350	±0.0069	80
RMS α (°)	±0.0145	±0.0038	74

Table 3. Self-calibration residual statistics.

Three separate scans of an independent set of 45 targets co-ordinated by total station were captured from different locations with the same resolution on the same day. These targets were co-ordinated by intersection from two instrument locations. A 900 mm Leica scale bar (σ = ±0.002 mm) was included in the network for scale definition. The mean co-ordinate precision (1σ) of the 45 targets from the 3D free network adjustment was ±0.5 mm in the horizontal and ±0.1 mm in height.

4.2 Accuracy Assessment without Corrections

In total, 120 points from the three independent scans were available for comparison. The targets ranged from 1.8 m to 10.4 m from the scanner throughout the full horizontal field of view. The elevation angle range was approximately ±60°, so the efficacy of the models for elevation-angle-dependent errors—which are among the largest errors—could be examined. An inner constraints (with the surveyed points defining the datum) rigid-body transformation adjustment of scanner observations was performed. Residuals (v) from these adjustments, hereafter referred to as differences, were used for the assessments that follow. Two cases were examined: without and with correction of the observations using the previously-derived APs.

Figure 4 is a plot of range differences as a function of range for the case without AP corrections applied. The results from all 3 scans are combined together for this and all subsequent plots in this section. The linear trend in this figure is primarily due to the un-modelled additive constant. A linear rather than a constant pattern occurs due to correlation between a_0 and the X_s and Y_s parameters, a mechanism that has been observed in the calibration datasets. Figure 5 shows the effect of the un-modelled elevation-angle-dependent rangefinder error, which is most evident in the left cluster that is concentrated below zero. The trend due to un-modelled collimation axis and trunnion axis errors is more difficult to see in Figure 6. When compared to Figure 9 (results with AP correction) it can be seen that the left and right clusters in Figure 6 are slightly concentrated below and above zero, respectively.

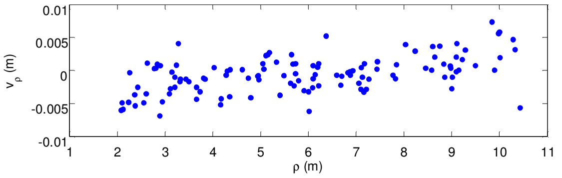

Figure 4. Range differences vs. range without AP correction.

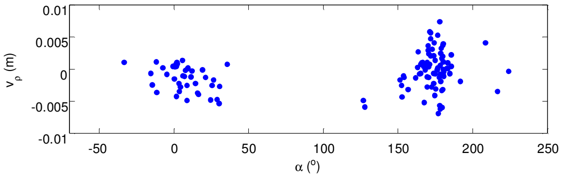

Figure 5. Range differences vs. elevation angle without AP correction.

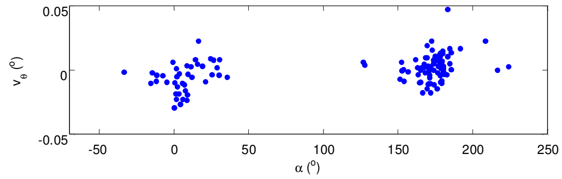

Figure 6. Horizontal direction differences vs. elevation angle without AP correction.

4.3 Accuracy Assessment with Corrections

Results from the case with AP corrections applied are plotted with same axis scales to allow direct comparison. Figure 7 shows the range difference plot, from which it is clear that the bias seen in Figure 4 has been removed as only random errors remain. Figure 8 demonstrates the model efficacy at removing the elevation-angle error in range and Figure 9 shows that the collimation axis and trunnion axis errors have been modelled effectively. In each case the residuals are more concentrated about zero than in Figures 4, 5 and 6.

Table 4 summarises the statistical outcomes of the accuracy assessment in terms of the RMS of both spherical and Cartesian co-ordinate differences. Improvement due to the correction with APs can be seen regardless of which set of co-ordinates is analysed. In contrast to the self-calibration results in Table 3, range improved the most. The RMSs of angular differences were lower than they were for self-calibration, which may be due to the more limited network geometry in terms of elevation angle range. Measured in terms of percentage of the 0.044° angular-sampling-interval, horizontal direction improved from 28% to 19%, and elevation angle improved from 15% to 10%.

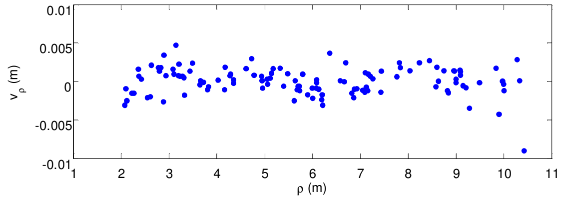

Figure 7. Range differences vs. range with AP correction.

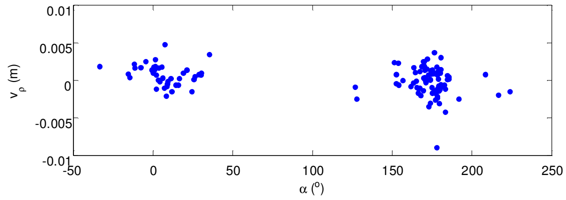

Figure 8. Range differences vs. elevation angle with AP correction.

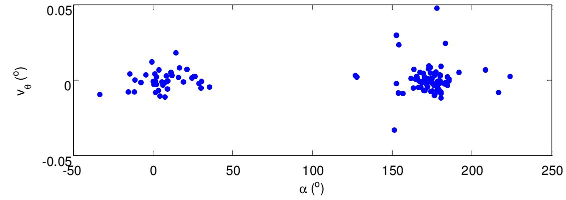

Figure 9. Horizontal direction differences vs. elevation angle with AP correction.

	Without Correction	Corrected	% Improvement
RMS ρ (m)	±0.0028	±0.0018	36
RMS θ (°)	±0.0123	±0.0086	30
RMS α (°)	±0.0065	±0.0045	31
RMS x (m)	±0.0023	±0.0018	23
RMS y (m)	±0.0022	±0.0016	52
RMS z (m)	±0.0011	±0.0006	44

Table 4. Check point statistics without and with AP corrections.

5. OTHER TESTING

5.1 Faro Parameters

Two similar self-calibration datasets, each with 8 scans in a 9 x 5.3 x 3 m laboratory with 134 targets were captured in October 2005. The first was captured under normal operating conditions. For the second, the preset Faro correction coefficients for angular errors were set to zero prior to data acquisition. The aim was to learn more about these parameters and to gain an understanding of why they do not completely remove the collimation axis and trunnion axis errors, as reported by Lichti and Franke (2005).

Some results from the self-calibration of the first dataset are presented in Figure 10, for which the b_1 and b_2 parameters were deliberately omitted from the calibration. The trends in the plot of horizontal-direction residuals as a function of elevation angle clearly show that the collimation axis and trunnion axis errors are not completely modelled by the Faro correction parameters. If these were modelled properly, Figure 10 would show only random noise. The b_1 and b_2 parameters that model these uncorrected errors estimated by our self-calibration software were 40″ and -146″, respectively.

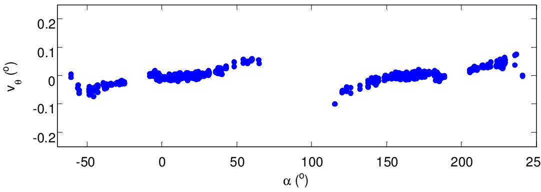

Figure 10. Collimation axis and trunnion axis errors un-modelled by the Faro calibration parameters.

Figure 11 is a plot of the same variables at the same scale for the second dataset, for which the Faro parameters were set to zero. Once again the b_1 and b_2 parameters were deliberately omitted from the calibration. Clearly the magnitude of the combined error in this case, which best represents the errors inherent in the system, is much larger. The self-calibration estimates were 185″ for b_1 and 276″ for b_2. Thus, the Faro calibration parameters under-correct for collimation axis error and over-correct for trunnion axis error, as they introduce a smaller error of opposite sign.

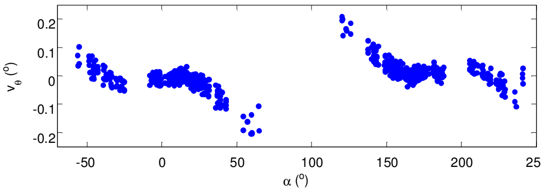

Figure 11. Un-modelled collimation axis and trunnion axis errors with Faro parameters set to zero.

5.2 Home Position Bias

Indoor repeatability testing under controlled conditions in June 2005 revealed a random bias in the home position (0° orientation) of the horizontal direction. This is most likely due to the mechanism that drives the scanner back to the home position after each scan. The A4-size Faro target mounted flatly on a diffuse white aluminium plate (500 mm x 500 mm x 2 mm) pictured in Figure 12 (a) was scanned 16 times at normal incidence. The image in Figure 12 (b) shows the superposition of two of the resulting point clouds. The 0.3° difference in the horizontal position of their centroid estimates (as determined by iQscene) is equivalent to 38 mm at the 7.25 m target range.

Figure 13 shows more detailed results. Here, the deviations from the sample mean are plotted for the spherical co-ordinates of the iQscene-determined centroid for each of the 16 repeat scans. The deviations in range and elevation angle are due to random noise whereas those for the horizontal direction—which are an order of magnitude larger than those for elevation angle—include the random home position bias. Five of the observations have a 0.2° residual whereas that of the others is -0.1°.

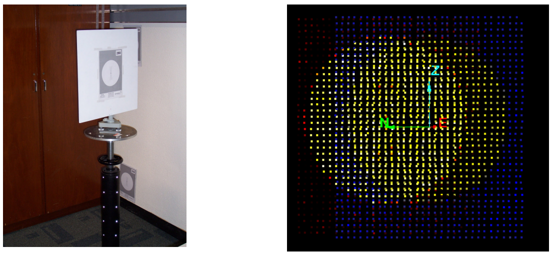

(a) (b)

Figure 12. (a) Repeat testing target setup. (b) Superposition of two scans of the same target captured from the same location.

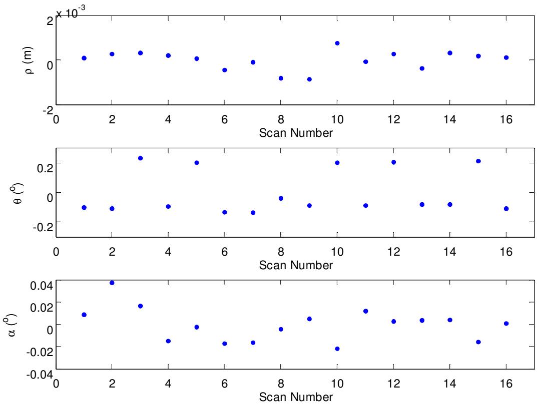

Figure 13. Repeat scan residuals.

Though a significant bias, it is not of concern in either self-calibration or target-based scanner orientation since in these cases the phase shift in horizontal direction is compensated by a corresponding change to the estimated κ rotation angle. It is of concern, though, for applications such as short-term deformation monitoring where the instrument position and orientation are assumed to be static during the capture of two or more epochs of data (i.e. they are not estimated). Unless the scanner is independently oriented for each dataset, the inferred horizontal deformation components could be biased.

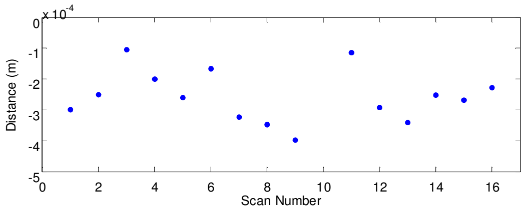

Figure 14. Distance between centroid and best-fit plane.

5.3 Centroid Bias

The dataset from the previous section was used to evaluate whether a range bias exists in the iQscene centroid determination. For each of the 16 repeat scans, the distance between the best fit plane of all data on the plane (Faro target plus the surrounding white background) and the iQsene centroid was calculated. The results are plotted in Figure 14, for which the mean is -0.24 mm and standard deviation ±0.11 mm. If it is hypothesised that the best-fit plane represents the true surface, then this small bias can be attributed to the centroid estimation algorithm. However, it is of no consequence since its effect is lumped into the rangefinder additive constant determined through self-calibration.

5.4 Scale Error Estimation

As mentioned previously, rangefinder scale can not be determined using the calibration approach outlined and must therefore be estimated by other means. Experience has shown that use of an outdoor EDM baseline is not optimal for this instrument due to its short maximum unambiguous range (76.7 m) and typical pillar spacing best suited to instruments with 10 m unit length. Instead, an indoor, certified tape calibration facility with shorter inter-monument spacing and controlled lighting and environmental conditions was utilised in February 2006. The facility consists of 13 marks and is 30 m long. Each monument, shown in Figure 15 (a), comprises a finely etched mark orthogonal to a recess in the surface against which a tape would be positioned. Eleven marks span the range 0 m to 10 m with the remaining two at 20 m and 30 m. The 95% precision estimates for the 12 inter-mark distances range from ±0.08 mm to ±0.29 mm, which are nearly an order of magnitude more precise than the Faro 880 rangefinder precision.

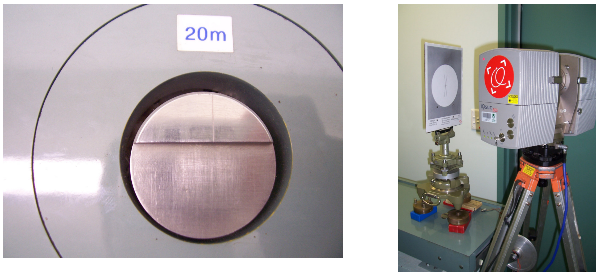

(a) (b)

Figure 15. (a) Calibration mark. (b) Instrument and target setup.

An A4-size Faro target was mounted to a Leica target, optically centred over each mark, as shown in Figure 15 (b), and scanned. Since the scanner can not be optically centred, it was set up at short distance from each end of the 'baseline' at the same height as the target. The iQscene-derived centroid co-ordinates were corrected using the APs from self-calibration then reduced to horizontal distances. Due to the 'eccentric' instrument setup, two unknown, scanner-to-endpoint distances had to be determined. Each could be independently estimated since the inter-mark distances were considered constants.

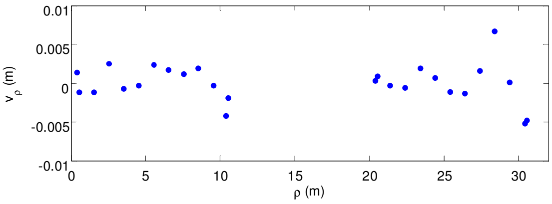

Figure 16. Indoor baseline testing range residuals.

Figure 16 shows the residuals between the known distances (plus scanner-to-endpoint distances) and the observed distances. Clearly no trends exist in the 26 data points; the scatter only resembles noise which suggests that there is neither a scale error nor long-period cyclic error in rangefinder. The RMS of residuals was ±0.0024 m.

6. CONCLUSIONS

This paper has presented recent advances in TLS error modelling and self-calibration. The effectiveness of these efforts has been demonstrated both internally in terms of residuals and externally by independent assessment. Improvements of up to 80% for self-calibration residual RMS and up to 36% of co-ordinate differences in the accuracy assessment were achieved.

Several important outcomes resulted form other testing conducted on the Faro TLS system. First, the previously-unknown nature of manufacturer-defined calibration terms for certain angular errors was revealed. They were found to inadequately model the collimation axis and trunnion axis errors. Second, a random bias in the instrument's home position was found through repeat testing. Third, a small centroid bias was uncovered by comparing the computed target position with best-fit plane. Fourth, no significant scale bias was found in the instrument, which is very important since this can not be determined by the proposed self-calibration procedure.

7. ACKNOWLEDGEMENTS

The authors gratefully acknowledge the assistance of Jochen Franke, Garth Johnson, Kwang-Ho Bae of Curtin University and Bob McCarthy and Brian Hugessen of the Department of Land Information Western Australia.

REFERENCES

Abmayr, T., G. Dalton, F. Hätrl, D. Hines, R. Liu, G. Hirzinger and C. Frölich, 2005. Standardization and visualization of 2.5D scanning data and color information by inverse mapping. In: *Optical 3-D Measurement Techniques VII*, Vienna, Austria, Vol. I, pp. 164-173.

Amiri Parian, J. and A. Grün, 2005. Integrated laser scanner and intensity image calibration and accuracy assessment. In: *The International Archives of the Photogrammetry, Remote Sensing and Spatial Information Sciences*, Enschede, The Netherlands, Vol. XXXVI, Part 3/W19, pp. 18-23.

Covell, P.C and J.M Rüeger, 1982. Multiplicity of cyclic errors in electro-optical distance meters. *Survey Review*. Vol. 26 (203), pp. 209-224.

Gielsdorf, F., A. Rietdorf and L. Gruendig, 2004. A Concept for the calibration of terrestrial laser scanners. In: *Proceedings of the FIG Working Week*, Athens, Greece. [On CD-ROM].

Kersten, T.P., H. Sternberg and K. Mechelke, 2005, Investigations into the accuracy behaviour of the terrestrial laser scanning system Mensi GS100. In: *Optical 3-D Measurement Techniques VII*, Vienna, Austria, Vol. I, pp. 122-131.

Lichti, D.D. and J. Franke, 2005. Self-calibration of the iQsun 880 laser scanner. In: *Optical 3-D Measurement Techniques VII*, Vienna, Austria, Vol. I, pp. 112-121.

Rüeger, J.M, 1990. Electronic Distance Measurement: an Introduction. 3rd edition. Springer-Verlang, Heidelberg, Germany, 266 pp.